

Article

Hybrid Fuel Cell—Supercritical CO₂ Brayton Cycle for CO₂ Sequestration-Ready Combined Heat and Power

Rhushikesh Ghotkar ¹, Ellen B. Stechel ² , Ivan Ermanoski ³ and Ryan J. Milcarek ^{1,*} 

¹ School for Engineering of Matter, Transport and Energy, Arizona State University, Tempe, AZ 85287-6106, USA; rghotkar1@asu.edu

² ASU LightWorks® and School of Molecular Sciences, Arizona State University, Tempe, AZ 85287-5402, USA; Ellen.Stechel@asu.edu

³ ASU LightWorks® and School of Sustainability, Arizona State University, Tempe, AZ 85287-5402, USA; Ivan.Ermanoski@asu.edu

* Correspondence: Ryan.Milcarek@asu.edu; Tel.: +1-480-965-2724

Received: 23 July 2020; Accepted: 22 September 2020; Published: 24 September 2020



Abstract: The low prices and its relatively low carbon intensity of natural gas have encouraged the coal replacement with natural gas power generation. Such a replacement reduces greenhouse gases and other emissions. To address the significant energy penalty of carbon dioxide (CO₂) sequestration in gas turbine systems, a novel high efficiency concept is proposed and analyzed, which integrates a flame-assisted fuel cell (FFC) with a supercritical CO₂ (sCO₂) Brayton cycle air separation. The air separation enables the exhaust from the system to be CO₂ sequestration-ready. The FFC provides the heat required for the sCO₂ cycle. Heat rejected from the sCO₂ cycle provides the heat required for adsorption-desorption pumping to isolate oxygen via air separation. The maximum electrical efficiency of the FFC sCO₂ turbine hybrid (FFCTH) without being CO₂ sequestration-ready is 60%, with the maximum penalty being 0.68% at a fuel-rich equivalence ratio (Φ) of 2.8, where Φ is proportional to fuel-air ratio. This electrical efficiency is higher than the standard sCO₂ cycle by 6.85%. The maximum power-to-heat ratio of the sequestration-ready FFCTH is 233 at a $\Phi = 2.8$. Even after including the air separation penalty, the electrical efficiency is higher than in previous studies.

Keywords: supercritical CO₂; combined heat and power; flame-assisted fuel cells; carbon sequestration; solid oxide fuel cell

1. Introduction

Over the past few decades, natural gas (NG) production in the USA has increased by 40% [1]. NG has been termed a “bridge fuel” between the fossil carbon-intensive electric grid of today and the low fossil carbon grid of the future [2–4]. Along with less carbon dioxide (CO₂) emissions per kWh [5,6], switching from coal to NG also provides several health benefits. Natural gas power plants emit less sulfur dioxide (SO₂) [7], nitrogen oxides (NO_x) [2], and primary particulate matter [2] when compared to coal-fired power plants. Emissions of primary particulate matter (PM_{2.5} and PM₁₀) have been linked to human mortality and morbidity [8–12]. Recent regulations have focused attention on reducing emissions and are drivers for a switch from coal to NG power plants [1,13].

Though NG plants have much lower emissions than coal, they still produce substantial amounts of CO₂—one of the most prominent greenhouse gas other than water vapor in the atmosphere [14]. Therefore, to minimize CO₂ emissions, while still maintaining dispatchability, it is important to address two aspects of power generation: (1) increasing power plant efficiency, and (2) sequestering CO₂.

An electrical efficiency frontrunner power cycle is the supercritical CO₂ (sCO₂) Brayton cycle. Further improving the efficiency will require hybrid approaches, including topping and/or bottoming cycles; one example is the use of solid oxide fuel cells (SOFCs) as a topping cycle.

Dual chambered solid oxide fuel cells (DC-SOFC) are highly efficient, but suffer from limited fuel flexibility due to carbon coking with hydrocarbon fuels [15]. Fuel reformers or catalysts address coking but increase complexity and cost. DC-SOFC also have low thermal endurance leading to sealant failure and performance reduction under cycling load [16,17], so they are not a good candidate for long-term practical applications.

Flame-assisted fuel cells (FFC), and the related direct flame fuel cells (DFFCs) [18–22], were developed to overcome the limitations of DC-SOFC [23–29]. In the FFC setup, fuel-rich combustion (i.e., partial oxidation) generates syngas (i.e., H_2 and CO), which generates power in the SOFC [28]. Lean combustion of the remaining fuel maximizes heat recovery [28,30]. Integration of FFC with NG fueled combustion subsystems can lead to improvements in thermal cycling and an increase in the overall system efficiency while reducing the complexity and cost compared to a DC-SOFC system [25,29,31]. Recently, a paper investigating the integration of FFC with an air Brayton cycle has shown a significant increase in net electrical efficiency due to the integration [32]. Along the same lines, the FFC with a sCO_2 turbine, proposed in this paper, aims to achieve electrical efficiency gains at a lower cost compared to integration with a traditional SOFC system.

Further decrease in CO_2 emissions can be achieved by CO_2 sequestration, which has been investigated recently [33–35]. Integrating CO_2 sequestration with common power cycles leads to efficiency and cost penalties [36,37], which must be minimized. The approach we examine here relies on low temperature (323–473 K depending on the material) thermally-driven adsorption/desorption cycle for air separation [38,39] to provide pure oxygen to the power cycle. Using pure oxygen produces an exhaust stream containing only CO_2 and water vapor, which after condensing the water vapor, is sequestration-ready. In the activation step of the sorption cycle, a high surface area solid sorbent with adsorbed oxygen is heated, leading to O_2 desorption. In the pumping step, oxygen from air exothermically chemisorbs on the surface (either molecular or dissociative) [38]. Due to the low temperature requirement, the heat required for the activation step can make use of the heat rejected by the sCO_2 cycle. With CO_2 removal from the exhaust, the FFC- sCO_2 turbine hybrid (FFCTH) can be a zero carbon emissions power and heat generation system.

Here, we analyze the combined approach to emissions-free, CO_2 sequestration-ready, NG power generation, via the integration of a FFC and sorption air separation, with a sCO_2 Brayton cycle. The FFC and sCO_2 turbine generates power; heat recovery makes this FFCTH a combined heat and power (CHP) system. This analysis investigates the benefits of the FFCTH integration showing a plausible path to zero emissions, high efficiency, combined heat, and power.

2. Theory

This section establishes the theory of the overall concept and the individual components in the FFCTH. We first show a detailed analysis of the contribution from each component in the overall system. Following this component analysis, we provide a description of the experimental setup for testing the FFC along with the materials and methods used to conduct the experiment. Lastly, we use the results from the experiments in the theoretical analysis to evaluate the concept further.

2.1. Theoretical Basis: sCO_2 Cycle, FFCs, Air Separation, and System Level

2.1.1. Standard sCO_2 Brayton Cycle

This section reviews the theory of a standard sCO_2 Brayton cycle with recuperation and recompression, to provide a baseline for performance of a standalone sCO_2 cycle. Figure 1 shows a schematic of a standard sCO_2 cycle with recuperation and recompression [40]. At state 1, 53% of CO_2 at a pressure of 7.5 MPa and a temperature of 300 K enters the system where it is compressed to a higher pressure and reaches state 2. Meanwhile, the secondary compressor compresses the rest of the CO_2 , which starts at the same pressure, but higher temperature and reaches state 2a.

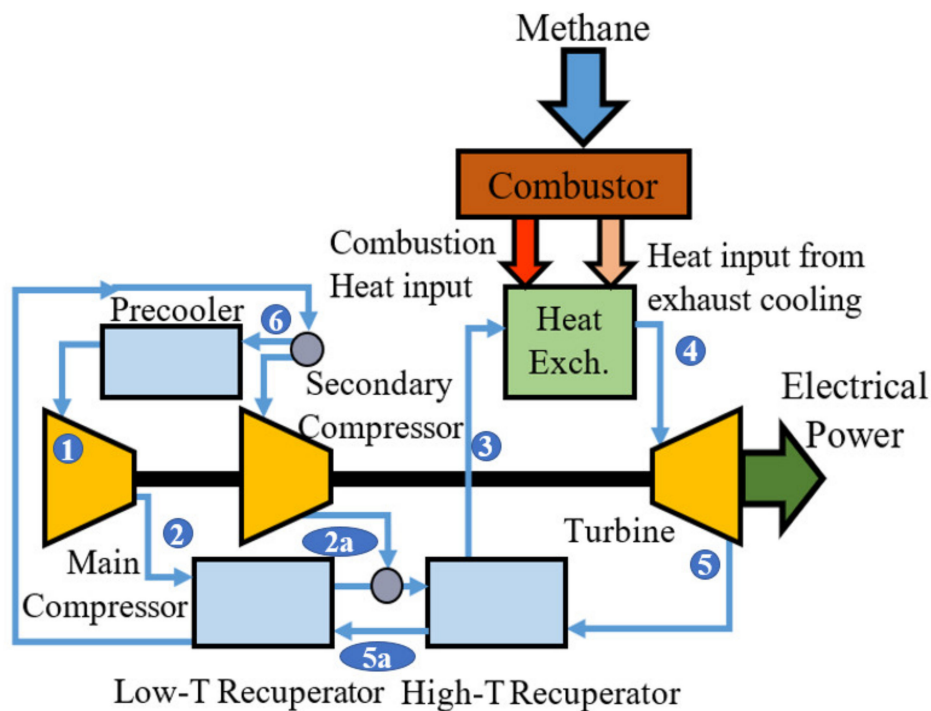


Figure 1. Schematic of a standard sCO₂ Brayton cycle with recuperation and recompression showing the various state points in the system.

The initial CO₂ from state 2 is preheated in the low temperature recuperator and reaches state 2a where the two CO₂ streams combine. The complete stream is then further preheated in the high temperature recuperator and reaches state 3. Further heat addition from external sources like combustion of a fuel or a concentrating solar thermal heat transfer fluid via a heat exchanger brings the CO₂ to state 4. For the purposes of the analysis here, we use combustion of methane to generate the heat in order to provide the most direct comparison with the FFCTH system. A turbine extracts mechanical energy from the sCO₂ stream between state 4 to state 5. The turbine exit stream preheats the incoming CO₂ streams in the high temperature recuperator, reaching state 5a, and in the low temperature recuperator, reaching state 6. Heat rejection to the environment or for external processing heating occurs in the pre-cooler, to return to state 1. Cooling the exhaust from the combustor and supplying thermal energy to the sCO₂ turbine cycle facilitates maximizing the electrical efficiency.

The electrical efficiency of the standard sCO₂ cycle (η_{SSGT}) given in Figure 1 is represented in Equation (1), where \dot{m}_{CO_2} is the total CO₂ mass flow rate in the cycle. The specific enthalpies of states 1, 2, 2a, 4, 5, and 6, are $h_1, h_2, h_{2a}, h_4, h_5,$ and h_6 , respectively. The coefficients 0.53 and 0.47 are the mass fraction of CO₂ entering the main compressor and secondary compressor, respectively. The mass flow rate of methane required to provide the necessary thermal energy is \dot{m}_f , and HHV_f is the higher heating value of methane. P_{CC} is the total electrical power required for CO₂ compression during sequestration. Previous literature has shown that the specific power required for compression and refrigeration of CO₂ for sequestration at 15 Bar is 107 kW/kg CO₂ [41], which is used in this work. This power is kept zero when sequestration is not assessed.

$$\eta_{SSGT} = \frac{\dot{m}_{CO_2} [(h_4 - h_5) - 0.47(h_{2a} - h_6) - 0.53(h_2 - h_1)] - P_{CC}}{\dot{m}_f HHV_f} \quad (1)$$

2.1.2. Flame-Assisted Fuel Cells

This section provides a theoretical model of the FFC, in which performance depends on the fuel-rich equivalence ratio (Φ), defined in Equation (2), as the independent variable. A more detailed FFC model is given in [42]. Here, n_{CH_4} and n_{O_2} are molar flow rates of methane and oxygen, respectively. The superscript 'S' denotes rates required for stoichiometric reaction. Thus, combustion is fuel-rich for $\Phi > 1$, fuel-lean for $\Phi < 1$, and stoichiometric for $\Phi = 1$.

$$\Phi = \frac{\frac{n_{\text{CH}_4}}{n_{\text{O}_2}}}{\frac{n_{\text{CH}_4}^s}{n_{\text{O}_2}^s}} \quad (2)$$

Figure 2 shows a schematic of a FFC with various reaction zones. The SOFC in the FFC configuration consists of a porous anode and cathode separated by a dense electrolyte layer. Partial oxidation of the fuel (i.e., methane in this study) and oxygen mixture sent to the fuel-rich pre-burner results in the generation of syngas ($\text{H}_2 + \text{CO}$). The syngas then diffuses into the anode where it reacts with the oxygen ions diffusing from the cathode side through the electrolyte to form CO_2 and water. After the fuel cell, remaining syngas combusts with oxygen, in the fuel-lean (excess oxygen reactant) after-burner and generates heat. The after-burner exhaust exits the fuel cell subsystem. The overall FFC subsystem generates heat during fuel-rich combustion, fuel cell electrochemical oxidation, and fuel-lean combustion.

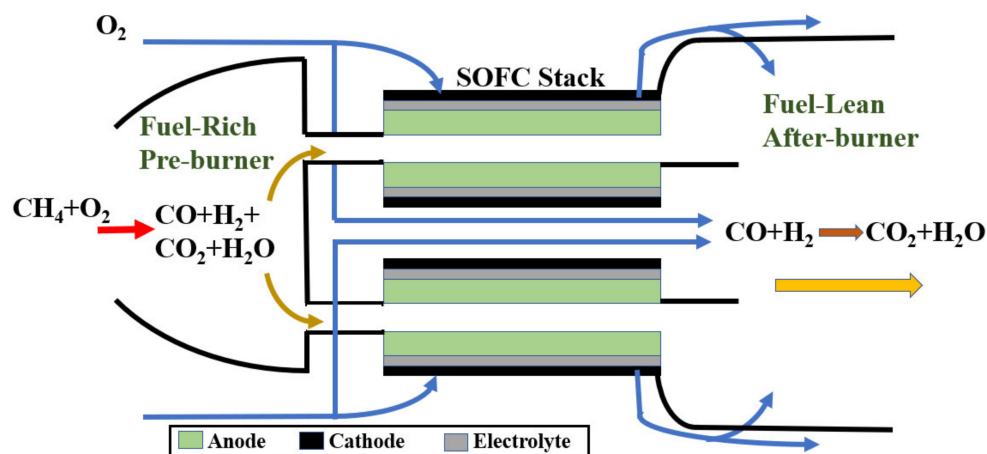


Figure 2. Schematic of a flame-assisted fuel cell (FFC).

The first reaction is the fuel-rich combustion of methane in oxygen. Equation (3) shows this reaction. Chemical equilibrium from a Gibbs minimization constrained by conservation of the elements determines the stoichiometry of the products for fuel-rich combustion, i.e., a , b , c , and d , for CO , H_2 , CO_2 , and H_2O , respectively.



The enthalpy released by the fuel-rich combustion reaction (ΔH_{RC}) can be calculated as shown in Equation (4), where \dot{m}_i is the mass flow rate for species i and h_i is the species specific enthalpy (i.e., per unit mass).

$$\Delta H_{\text{RC}} = \dot{m}_{\text{CO}} h_{\text{CO}} + \dot{m}_{\text{CO}_2} h_{\text{CO}_2} + \dot{m}_{\text{H}_2\text{O}} h_{\text{H}_2\text{O}} + \dot{m}_{\text{H}_2} h_{\text{H}_2} - \dot{m}_{\text{CH}_4} h_{\text{CH}_4} \quad (4)$$

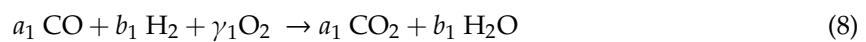
Various losses give rise to three key efficiency definitions in the FFC subsystem. Those include the fuel utilization efficiency (η_{fu}), the fuel cell conversion efficiency (η_{fc}), and the overall efficiency (η_{ov}). Equations (5)–(7) define each efficiency, respectively.

$$\eta_{fu} = \frac{\text{Syngas electrochemically oxidized in FFC}}{\text{Total Syngas available in exhaust}} \quad (5)$$

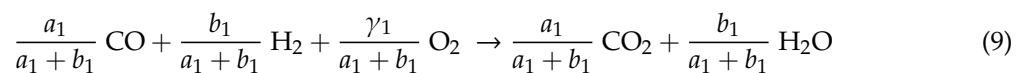
$$\eta_{fc} = \frac{\text{Electrical power generated by FFC}}{\text{Total Chemical energy of the available syngas}} \quad (6)$$

$$\eta_{ov} = \frac{\text{Electrical power generated by fuel cell}}{\text{Chemical energy from the hydrocarbon fuel}} \quad (7)$$

FFC electrochemically oxidized both H_2 and CO to generate electric power. Equation (8) shows the effective fuel cell reaction, in which the coefficients a_1 , b_1 , and γ_1 depend upon the a and b stoichiometric coefficients from Equation (3) and the fuel utilization efficiency of the FFC (Equation (5)).



Writing the reaction Equation (8) per mole of syngas leads to Equation (9).



The mole specific standard Gibbs' free energy released by reaction Equation (8) (Δg°_{FC}) and the temperature is used to calculate the reversible cell potential (V_{rev}) of the fuel cell as shown in Equation (10). In Equation (10), R is the universal gas constant, T is absolute temperature (in Kelvin), and K is the equilibrium constant of reaction in Equation (8). The mole specific enthalpy of reaction (8) (Δh_{FC}) is used to calculate the thermo-neutral potential (V_{th}) as shown in Equation (11) where n is the number of electrons released per mole of fuel in the fuel cell reaction (two electrons per mole of syngas) and F is Faraday's constant.

$$V_{rev} = \frac{-\Delta g^{\circ}_{FC}}{nF} - \frac{RT}{nF} \ln(K) \quad (10)$$

$$V_{th} = \frac{-\Delta h_{FC}}{nF} \quad (11)$$

The equilibrium constant is calculated as shown in Equation (12) where P_i/P is the ratio of partial pressure of species i and y_i/y_{syn} is the ratio of coefficients of species i in reaction Equation (8). The ratio of partial pressures in the subsystem is equal to the mole fraction of the components, assuming ideal gas behavior.

$$K = \prod_{i=1}^N \left(\frac{P_i}{P} \right)^{\frac{y_i}{y_{syn}}} \quad (12)$$

For the fuel cell reaction, Equation (13) shows how to determine the equilibrium constant, where X_i is the mole fraction of species ' i '.

$$K = X_{H_2}^{\left(\frac{-b}{a+b}\right)} X_{O_2}^{\left(\frac{-\gamma}{a+b}\right)} X_{CO}^{\left(\frac{-a}{a+b}\right)} \quad (13)$$

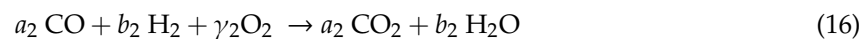
Equation (14) shows the power generated by the fuel cell (P_{fc}), where η_{fu} is the fuel utilization efficiency, η_{fc} is the fuel cell efficiency, \dot{n}_k is the molar flow rate of species ' k ' (CO or H_2) in the fuel-rich exhaust, $\Delta g_{CO,CO_2}$ and $\Delta g_{H_2,H_2O}$ are the mole specific Gibbs' free energies released from the oxidation of CO and H_2 , respectively.

$$P_{fc} = -\eta_{fu} \eta_{fc} (\dot{n}_{CO} \Delta g_{CO,CO_2} + \dot{n}_{H_2} \Delta g_{H_2,H_2O}) \quad (14)$$

Equation (15) shows the total heat released by the combined fuel cell reactions; $\Delta h_{\text{CO,CO}_2}$ and $\Delta h_{\text{H}_2,\text{H}_2\text{O}}$ are the mole specific enthalpy changes from the oxidation of CO and H₂, respectively.

$$H_{fc} = -\eta_{fu} \cdot (1 - \eta_{fc}) \cdot (\dot{n}_{\text{CO}} \Delta h_{\text{CO,CO}_2} + \dot{n}_{\text{H}_2} \Delta h_{\text{H}_2,\text{H}_2\text{O}}) \quad (15)$$

After the fuel cell, the remaining fuel passes into the fuel-lean combustion chamber to generate more thermal energy for transfer to the sCO₂ stream via an indirect heat exchanger. Equation (16) shows the fuel-lean combustion reaction. In Equation (16), the stoichiometric coefficients a_2 , b_2 , and γ_2 depend on stoichiometry a and b from Equation (3) and on the η_{fu} . Thus, if the fuel-rich combustion produces b moles of H₂ and a moles of CO and b_1 and a_1 moles of H₂ and CO, respectively, react in the fuel cell reaction, then a_2 equals the difference between a and a_1 and b_2 equals the difference between b and b_1 . Fixing the Φ of the fuel-lean combustion determines the value of γ_2 . The assumption and expectation is that CO₂ and H₂O generated in the fuel-rich combustion, FFC, and the fuel-lean combustion reactions remain unreacted downstream of when they are produced.



2.1.3. FFC sCO₂ Turbine Hybrid with and without Carbon Sequestration

Figure 3 shows a schematic of the proposed FFCTH system, where the sCO₂ turbine receives heat input from the FFC via an indirect heat exchanger. The optional air separation unit provides oxygen to the FFC and after-burner, with the resulting exhaust requiring only water removal to be sequestration-ready.

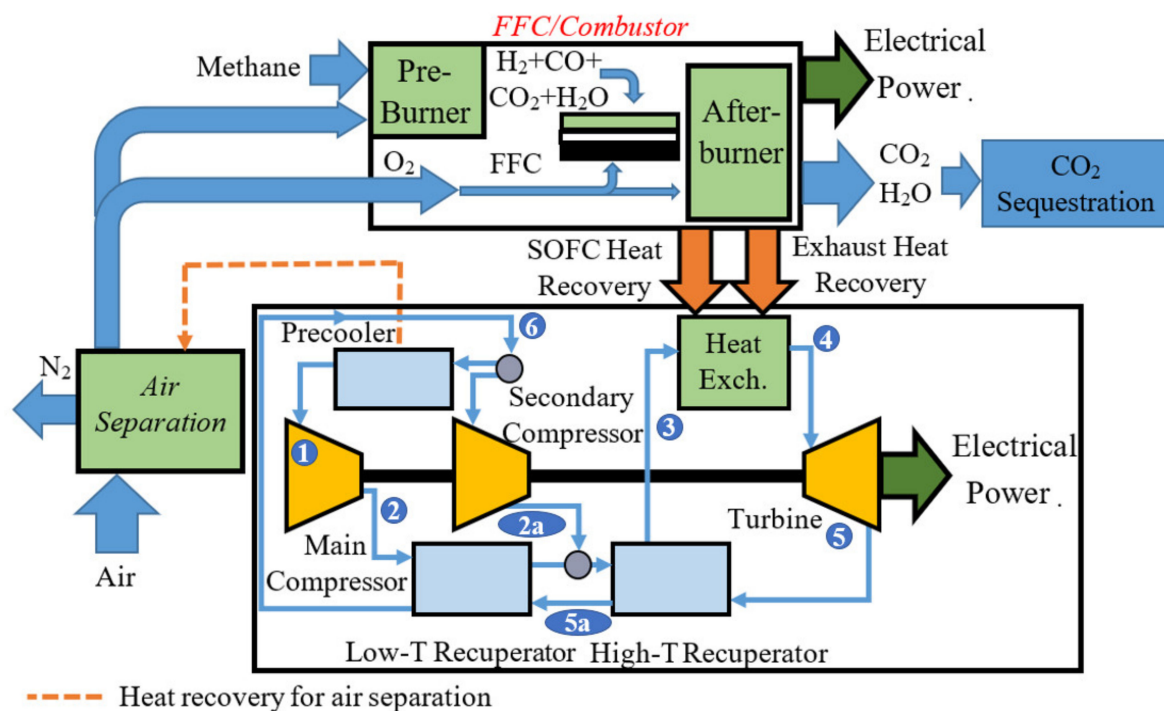


Figure 3. Schematic of the proposed FFC integrated sCO₂ turbine hybrid.

Use of FFC, instead of a conventional DC-SOFC, significantly reduces system complexity and size. The FFCTH has several tunable parameters, such as Φ , the FFC operating voltage/current, the air separation unit, and sCO₂ cycle variables. Examples of the latter are the pressure ratio and the turbine inlet temperature. All these tunable variables enable optimizing for a high power-to-heat ratio (P/H), high electrical efficiencies, and/or high thermal efficiencies. One key advantage of the system proposed

here is that the heat rejected from the pre-cooler can drive the sorption/desorption based air separation unit, thus making this system self-sustained and powered by one fuel source and one injection point. The efficiency of the sorption/desorption based air separation unit is assumed to be in the acceptable range. This assumption applies due to the various tunable state points in the cycle and parameters in the system depending upon the materials used for air separation. The state points of the sCO₂ cycle remain the same as shown in Figure 1 with two additional components: (1) heat recovery from the FFC subsystem and (2) air separation from a sorption unit.

To identify the advantages and drawbacks of redesigning so that the system can be CO₂ sequestration-ready, we theoretically analyzed this system with and without air separation. Without separation, the FFC subsystem uses air, whereas with separation it produces and utilizes pure oxygen. We compare the system efficiencies, the fuel requirement, and the P/H for cases with and without the FFC integrated and with and without sorption-based air separation. Equation (17) shows the electrical efficiency of the FFC integrated sCO₂ turbine FFCTH (η_{FFCGT}), where P_{FFC} and P_{CO_2GT} is the power generated by FFC and by the sCO₂ turbine cycle, respectively. The heat required for the air separation unit is taken from the heat rejected in the sCO₂ cycle pre-cooler (states 6 to 1). The electrical efficiency of the FFCTH is given by Equation (17).

$$\eta_{FFCGT} = \frac{P_{FFC} + P_{CO_2GT} - P_{CC}}{\dot{m}_f HHV_f} \quad (17)$$

3. Experimental

An experimental assessment and analysis of the FFC performance operating in methane and oxygen fuel-rich combustion exhaust provided data to calibrate and enable simulation of the FFCTH system. Figure 4 shows the schematic of the experimental setup. Use of mass flow controllers regulated the flow of the gases. Connecting the fuel lines for CO and H₂ to flame arrestors mitigates and avoids flashback risk.

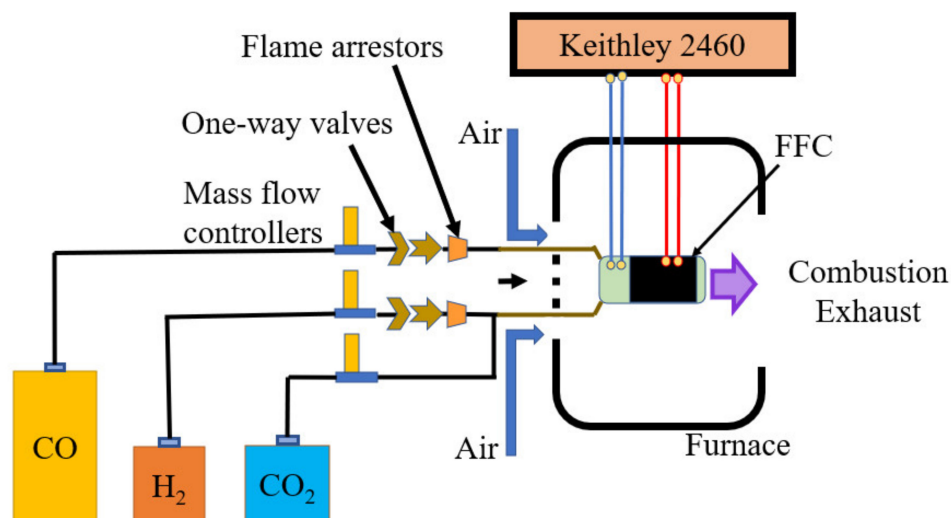


Figure 4. Schematic of the experimental setup with gases mixture used for model exhaust.

The flow rates of the gases used in the experiment (CO, H₂, CO₂) were calculated using chemical equilibrium, from NASA Chemical Equilibrium and Applications (CEA) [43], for the combustion exhaust composition at a constant inlet fuel flow rate of 0.066 mg·s⁻¹. Methane was used as an approximation for natural gas since natural gas is up to 90% methane by molar content [44] and thus, using methane instead of natural gas would not lead to significant departure from the natural gas case. Sulfur impurities will need to be removed from the natural gas before its use in the fuel cell due to

poisoning effect on the anode. Other hydrocarbon impurities are not expected to damage the fuel cell since they are reformed in the fuel-rich pre-burner. Tables 1 and 2 show the NASA CEA exhaust composition for combustion of methane in air and methane in oxygen, respectively. The term used for this exhaust composition, when obtained from chemical equilibrium, is ‘model fuel-rich exhaust’. The case of methane in air serves as a base case for comparison; however, the experiment used only the model fuel-rich exhaust for methane in oxygen as Table 2 shows. Since it is difficult to work with steam, and since steam should be non-reactive electrochemically, increasing the CO₂ molar flow serves to eliminate while compensating steam from the experiment. Thus, CO₂ molar flow rate in the experiment was the same total (steam plus CO₂) as in the proposed concept.

Table 1. NASA CEA exhaust composition of methane and air for different Φ .

Φ	CO (mL·min ⁻¹)	H ₂ (mL·min ⁻¹)	CO ₂ (mL·min ⁻¹)	H ₂ O (mL·min ⁻¹)	N ₂ (mL·min ⁻¹)
1.20	0.05	0.03	0.05	0.18	0.66
1.40	0.08	0.06	0.04	0.17	0.63
1.60	0.10	0.09	0.03	0.16	0.60
1.80	0.12	0.13	0.02	0.15	0.57
2.00	0.13	0.17	0.02	0.13	0.55
2.20	0.14	0.20	0.02	0.11	0.53
2.40	0.15	0.23	0.01	0.09	0.51
2.60	0.16	0.26	0.01	0.08	0.49
2.80	0.17	0.29	0.01	0.06	0.47

Table 2. NASA CEA exhaust composition of methane and oxygen for different Φ .

Φ	CO (mL·min ⁻¹)	H ₂ (mL·min ⁻¹)	CO ₂ (mL·min ⁻¹)	Total (mL·min ⁻¹)
1.20	0.2672	0.1560	0.0848	0.4715
1.40	0.2855	0.2000	0.0695	0.4333
1.60	0.2981	0.2503	0.0555	0.3899
1.80	0.3061	0.3053	0.0435	0.3418
2.00	0.3110	0.3614	0.0341	0.2921
2.20	0.3141	0.4142	0.0272	0.2444
2.40	0.3163	0.4612	0.0222	0.2010
2.60	0.3182	0.5020	0.0185	0.1625
2.80	0.3201	0.5369	0.0158	0.1289

Equation (18) shows the formula to calculate the volumetric flow rate of species ‘*i*’ as a function of Φ . In Equation (18), X_i and X_{CH_4} are the mole fractions of species ‘*i*’ and methane, respectively, obtained from Table 2 at the respective Φ . V_{mol} is the molar volume of an ideal gas at 298 K, 1 bar pressure. Table 3 shows the flow rates subsequently obtained. The gases were all mixed and sent to the FFC subsystem inside a furnace at 1073 K. Previous experiments have shown that the ionic and electronic conductivity of the electrodes and the ionic conductivity of the electrolyte are high at a temperature of 1073 K and above [16]. Furthermore, carbon deposition due to the carbon monoxide disproportionation reaction ($2\text{CO} \rightarrow \text{C} + \text{CO}_2$) is less favorable at operating temperatures of 1073 K and higher [16]. Thus, a temperature of 1073 K was chosen for the experiments. Air in the furnace was supplied to the fuel cell cathode.

$$V_i = \frac{\dot{n}_f}{X_{\text{CH}_4}} \times X_i \times V_{mol} \quad (18)$$

Table 3. Flow rates of gases used in the experiment at different Φ .

Φ	CO (mL·min ⁻¹)	H ₂ (mL·min ⁻¹)	CO ₂ (mL·min ⁻¹)	Total (mL·min ⁻¹)
1.20	3.33	1.94	7.18	12.45
1.40	3.81	2.68	6.87	13.36
1.60	4.22	3.55	6.40	14.17
1.80	4.55	4.55	5.78	14.88
2.00	4.82	5.59	5.06	15.47
2.20	5.00	6.61	4.33	15.94
2.40	5.15	7.51	3.63	16.29
2.60	5.25	8.28	2.96	16.49
2.80	5.32	8.93	2.38	16.63

Fuel Cell Fabrication

Fabrication methods for the FFC anode (NiO + YSZ, (Y₂O₃)_{0.08}(ZrO₂)_{0.92}) and the electrolyte (YSZ, ~22 μ m thick) used in this study were reported previously in the literature [24]. Pre-firing of the anode occurred at 1373 K. The electrolyte was dip coated on the anode and sintered at 1673 K for four hours. A buffer layer of Sm_{0.20}Ce_{0.80}O_{2-x} (SDC) was deposited onto the electrolyte using spray deposition [45]. An SDC+LSCF (La_{0.6}Sr_{0.4})_{0.95}Co_{0.2}0Fe_{0.8}O_{3-x}) cathode was deposited onto the buffer layer using dip coating, later dried and sintered at 1373 K for two hours. The final internal diameter of the tubular FFC is 2.2 mm and the outer diameter is 3.3 mm. The current collectors on the cathode and anode use silver wire and gold paste. The total active area of the cell is 4.32 cm². A source meter (Keithley 2460) is connected to the anode and cathode current collector. We used the current-voltage method with a four-probe technique to obtain the polarization curve and the power density.

4. Results and Discussion

4.1. Fuel Cell Performance

Figure 5 shows the performance of the FFC operating at 1073 K with a simulated methane/oxygen fuel-rich combustion exhaust composition between the Φ of 1.2 to 2.8 and flow rates shown in Table 3. A maximum Φ of 2.8 was chosen as carbon formation becomes thermodynamically favorable at higher Φ and peak hydrogen concentration occurs near this Φ . Figure 5 shows that significant power densities were achieved at all Φ .

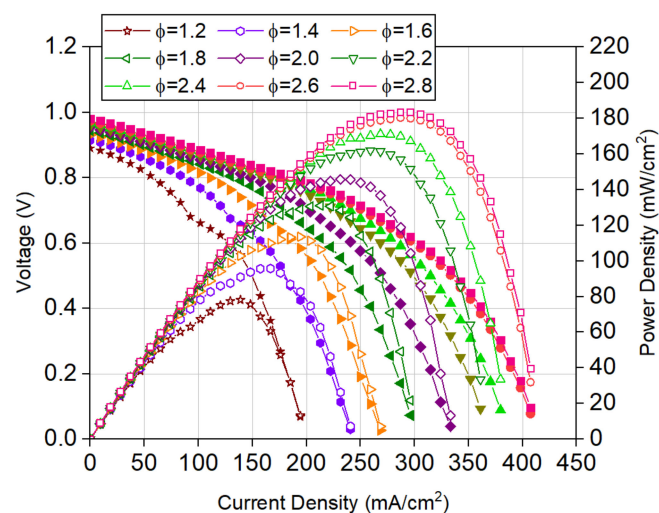


Figure 5. Modeling results for the FFC operating voltages and power density at 1073 K using a model fuel-rich exhaust composition between 1.2 and 2.8.

The significant change in FFC power density shown in Figure 5 is due to a change in polarization at different Φ . At lower current densities ($<100 \text{ mA/cm}^2$), the slope of the polarization curves remains similar at all Φ indicating dominant ohmic losses. At higher current densities, the polarization losses increase as Φ decreases. This happens because as the Φ decreases, the concentration of syngas in the combustion exhaust decreases, as Table 2 shows, leading to higher concentration losses. There are no significant activation losses at any Φ . As a result of changes in polarization, the power density at each current density increases as the Φ increases. As the Φ increases, more syngas is available in the combustion exhaust leading to larger Gibbs' free energy released, which in turn leads to less concentration losses and more total power being generated in the FFC. At an operating voltage of 0.6 V, the maximum power density of 183 mW/cm^2 occurs at a Φ of 2.8. This power density result ($<200 \text{ mW/cm}^2$) may not seem impressive on its own; however, consideration of the fuel-utilization efficiencies achieved during the experiment does give it more significance.

The fuel utilization efficiencies reached during the experiment are significantly higher than those found in literature for FFCs [16,24,42,46]. For example, a fuel utilization of 75% at Φ of 1.2 and 63% at Φ of 2.8 is obtained at an operating voltage of 0.6 V. Low flow rates and the controlled experiment in the furnace are the primary reasons for the high fuel utilization observed. Experiments were also conducted for a FFC operating in methane/air fuel-rich combustion exhaust and similar operating characteristics, fuel utilization, and fuel cell efficiency were obtained. The model, presented below, uses experimental parameters of fuel utilization and fuel cell efficiency for the FFC operation in methane/oxygen and methane/air fuel-rich combustion exhaust.

It is important to consider the validity of the FFC model described earlier for prediction of experimental results. From the results in Figure 5, the FFC open circuit voltage shows a clear increasing trend with Φ due to decreased Nernstian loss, as predicted by Equation (10). Figure 6 shows that the analytically calculated reversible cell potential and the open circuit voltage increase with increase in Φ due to increase in the syngas concentration in the fuel-rich combustion exhaust. This comparison indicates that the FFC model is in approximate agreement ($<5\%$ variation at all Φ) with the experimental results validating the theoretical model described in the paper.

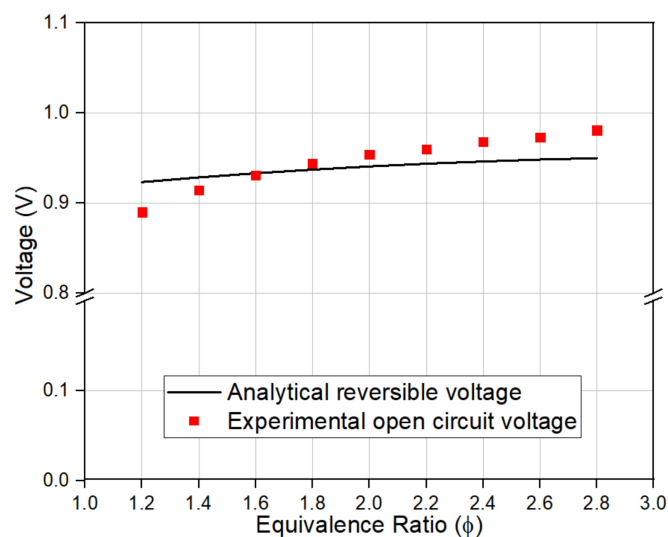


Figure 6. Comparison of analytically calculated reversible voltage and experimentally obtained open circuit voltage.

4.2. sCO₂ Turbine Performance with and without an Integrated FFC Subsystem

The computations for the FFCTH assumed that the FFC would achieve similar performance when scaled to design power as it did during the experiment. All thermochemical properties of gases were taken from NIST (Gaithersburg, MD, USA) software MINI-REFPROP [47].

To isolate the effects of integrating the FFC system with the standard sCO₂ cycle, the total power generated by the turbine system alone was held constant at 6 MW. To generate this power, Table 4 lists the temperature and pressure of various state points as defined in Figure 1.

Table 4. Temperatures and pressures of the state points in the sCO₂ cycle.

State Point	Temperature (K)	Pressure (MPa)
1	300	7.5
2	318	20
2a	414	20
3	733	20
4	913	20
5	780	7.5
5a	452	7.5
6	331	7.5

The state points in Table 4 were taken from a previous sCO₂ power cycle [40]. The mass flow rate of CO₂ required to generate 6 MW of power is 48.35 kg/s. The total amount of heat rejected from the sCO₂ turbine system is 4.81 MW. The compression ratio in the system is 2.66. With these parameters, we evaluated the performance of an integrated FFC system, which is able to provide the heat required by sCO₂ cycle. Air or oxygen is the oxidant for the FFC system. The oxygen case enables sequestration-ready exhaust from the FFC system. The heat rejected from the pre-cooler (states 6 to 1 in Figure 3) provides heat to separate oxygen from air using a thermally driven adsorption/desorption cycle [38]. If the heat rejected from the sCO₂ cycle is not enough to separate enough oxygen for the FFC system, we adjusted the FFC operating voltage to enable more heat rejection. Also note that the efficiency of the air-separation is assumed to be acceptable in the design. The flexibility of the cycle state points to give us this unique opportunity of analyzing this cycle and the assumption is thus justified. The state points will need to be modified depending upon the specific material used for adsorption–desorption pumping of oxygen for air separation [38,39]. The fixed parameters used in the analysis is shown in Table 5.

Table 5. Summary of the fixed parameters used in the analysis.

Property	Value
Power generated by standard supercritical CO ₂ turbine cycle	6 MW
Efficiency of the standard supercritical CO ₂ turbine cycle (based on states 1–6)	53.14%
Compression ratio	2.66

The fuel flowrate requirement of the FFCTH and its variation with Φ was assessed. The initial conditions for air (or oxygen) entering the fuel-rich combustion chamber of the FFC is 1 bar and 298 K. The Φ of the fuel-rich preburner varies, while Φ of the fuel-lean after-burner remains constant at 0.8. The assumed efficiency for the heat exchangers in the system is 90%. η_{fu} and η_{fc} (fixed at 0.7 and 0.5, respectively) are the average experimentally measured results over all Φ . Figure 7 shows the flow rate of methane required to generate the heat (10.8 MW) from the FFC with and without being CO₂ sequestration-ready. Figure 7 shows the base-case fuel-flow required to meet the heat requirements with a standard sCO₂ turbine cycle (Figure 1).

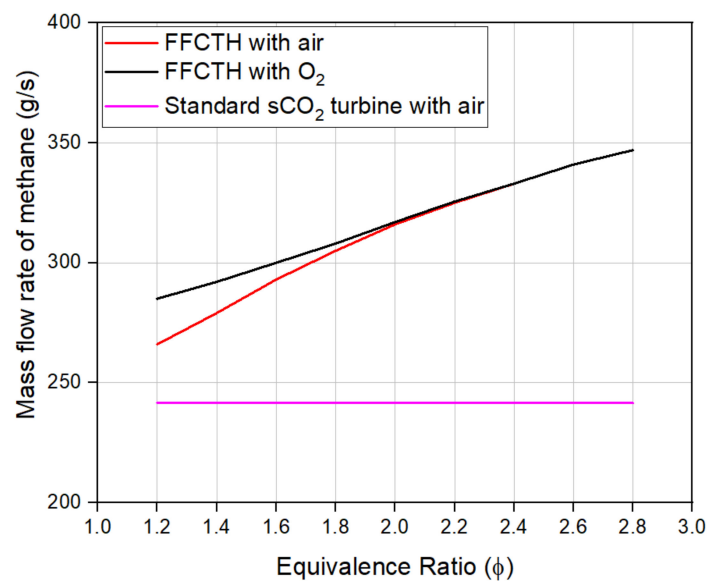


Figure 7. Flow rates of methane required to produce the required amount of heat for sCO₂ cycle with air and oxygen oxidizers for different Φ .

As shown in Figure 7, at all Φ the fuel flow required for the standard sCO₂ cycle is lower than the fuel flow for the FFCTH with and without being CO₂ sequestration-ready. In the standard sCO₂ cycle case, the fuels chemical energy is converted to heat and then to the sCO₂ cycle via the heat exchanger. Thus, the standard cycle requires less fuel, but also produces less power than in the case of the integrated FFC. The standard sCO₂ cycle operates at a fixed Φ of 0.8 as all of the heat released in the combustor transfers to the working fluid. This fuel flow result shows that more methane is required for the sequestration-ready FFCTH power generation compared to the sCO₂ cycle because the electrical power generated by the sCO₂ is fixed at 6 MW. However, the electrical efficiency of the FFCTH is higher overall, which will be shown below.

When integrating the FFC with the sCO₂ cycle, the amount of methane required to provide the necessary heat increases with Φ . This increase happens because as Φ increases a larger portion of the incoming fuel energy converts to electric power in the FFC due to the constant fuel utilization efficiency. To make up for the larger power generation, more fuel is necessary to meet the heat requirement. Thus, even though the FFCTH requires more methane flow to operate, it is important to consider the electrical efficiency (described in later sections) of the setup in order to establish the significance of these results. It also shows why the comparison of methane flow rate of FFCTH with standard sCO₂ turbine cycle alone can be misleading.

Figure 7 also shows that the fuel needed to meet the heat requirement is slightly higher with oxygen (CO₂ sequestration-ready case) than with air at lower Φ (7% higher at $\Phi = 1.2$). At higher Φ (>2), the fuel flow rates converge to the same value. To understand the reason for this trend, it is important to consider the syngas concentration of the fuel-rich combustion exhaust with air compared to with oxygen. For the fuel-rich combustion exhaust concentrations for methane with air and oxygen, we refer back to Tables 1 and 2. To maintain consistency for the purpose of the comparison, the nitrogen is removed, and the rest of the concentrations are rescaled, so they sum to 1. Table 6 shows these scaled concentrations.

Table 6. NASA CEA fuel-rich exhaust compositions for methane in air scaled to 1 without nitrogen.

Φ	CO	H ₂	CO ₂	H ₂ O
1.20	0.17	0.09	0.17	0.57
1.40	0.23	0.16	0.11	0.50
1.60	0.26	0.24	0.08	0.42
1.80	0.28	0.31	0.06	0.35
2.00	0.29	0.38	0.04	0.29
2.20	0.30	0.43	0.03	0.24
2.40	0.31	0.47	0.03	0.19
2.60	0.31	0.51	0.02	0.16
2.80	0.31	0.54	0.02	0.12

Figure 8 shows the trend in the variation of scaled syngas concentrations in the fuel-rich exhaust for methane combustion in air and oxygen. It is evident that the trend in Figure 7 matches the trend in the syngas composition of the fuel-rich combustion exhaust. The syngas oxidizes electrochemically and produces power in the FFC at an assumed constant fuel utilization. Hence, when the flow rates are equal, the higher syngas concentration for the methane/oxygen case will result in more electricity generation due to the constant fuel utilization in the FFC. Higher electricity generation for the methane/oxygen case will require a high flow rate (shown in Figure 7) in order to meet the thermal energy requirement of the sCO₂ bottoming cycle.

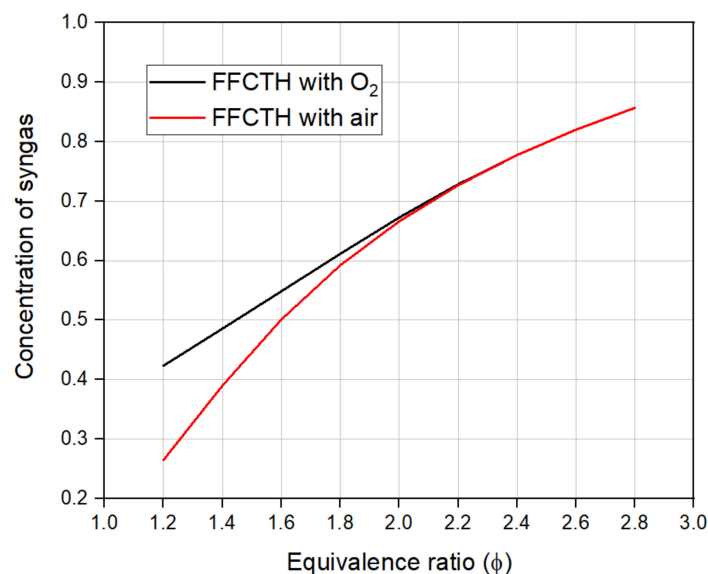
**Figure 8.** Syngas concentration in the fuel-rich combustion exhaust for methane combustion in air (without nitrogen and scaled to 1) compared to methane combustion in oxygen against increasing Φ .

Figure 9 shows the power generated by the sCO₂ cycle with oxygen and with air for the FFCTH. As a base case, Figure 9 shows the power generated by the standard sCO₂ turbine cycle. We note that the power generated in the oxygen case includes the electrical power penalty required for sequestration (i.e., compression) of the exhaust CO₂, as well as the air separation.

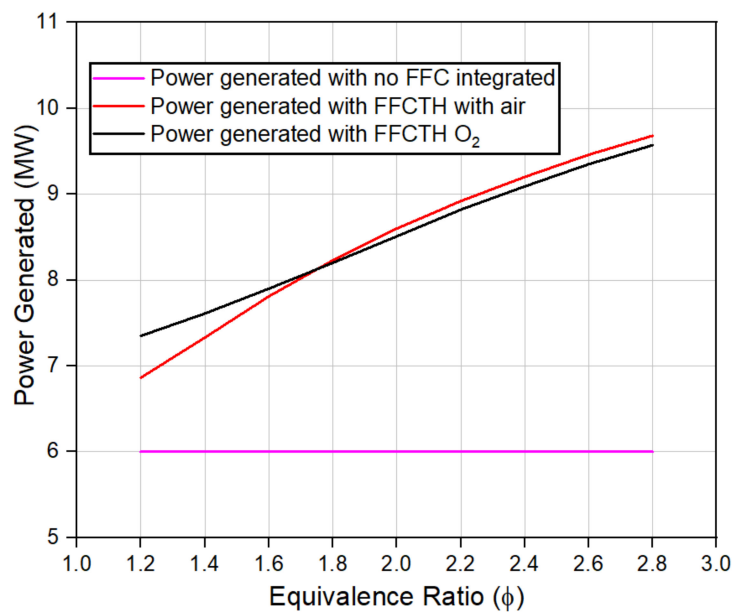


Figure 9. Comparison of the power generated by the sCO₂ turbine with and without FFC integrated and with and without being CO₂ sequestration-ready.

As shown in Figure 9, the power generated by the FFCTH increases with increasing Φ . This increase occurs because increasing the Φ increases the concentration of syngas in the fuel-rich combustion exhaust as shown in Table 1. Electrochemical oxidation of the syngas generates power; hence, more syngas leads to more electrical power generated as long as the fuel utilization remains high. Figure 5 shows the same trend for the experimental results, which confirms the trend and explains the model results.

The total power generated by the FFCTH system with and without being CO₂ sequestration-ready follows a slightly different trend than the one in Figure 7. This difference is primarily due to the compression penalty for making the exhaust CO₂ sequestration-ready. The power required for sequestration is small (0.1 MW) in comparison to the total power generated (~9.6 MW) at $\Phi = 2.8$. The total power generated by the FFCTH with being CO₂ sequestration-ready is 7% higher at $\Phi = 1.2$ and 1.2% lower at $\Phi = 2.8$ compared with no sequestration intent. It can also be seen that the total power generated by the FFCTH is significantly higher (~60% higher at $\Phi = 2.8$) compared to the standard sCO₂ turbine due to a large portion of the total power being generated by the FFC and the higher methane flow rate. Thus, analytical results show that the power generated by various cycles considered follows a slightly different trend than the trend for methane flow rate described earlier.

Figure 10 shows the variation of the electrical efficiency of the FFCTH system with and without CO₂ sequestration compared to the electrical efficiency of the standard sCO₂ turbine system with and without CO₂ sequestration. The standard sCO₂ turbine system was assessed with and without carbon-sequestration to assess the penalty for the baseline case. As expected, the electrical efficiency of the FFCTH system and the standard sCO₂ cycle is higher without sequestration than with sequestration.

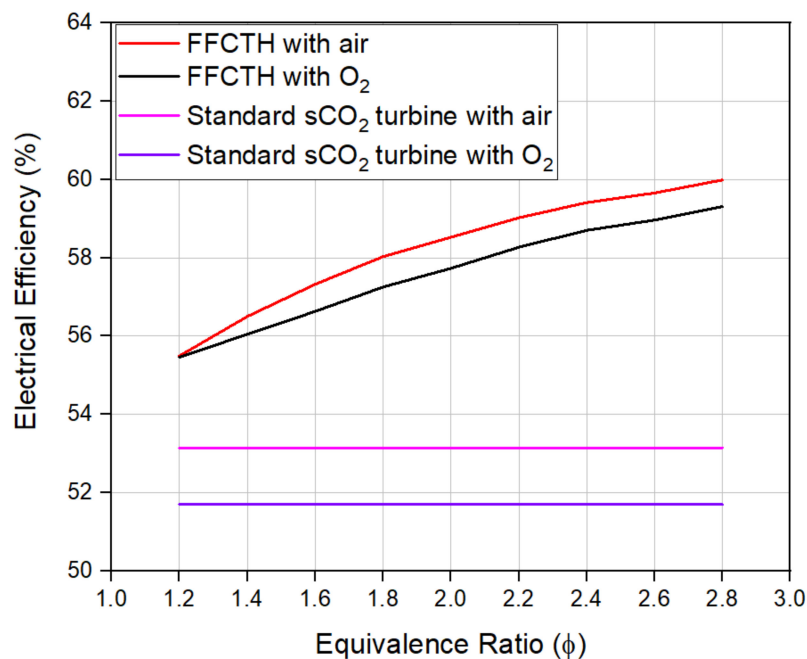


Figure 10. Comparison of the electrical efficiencies of the sCO₂ system with and without the FFC integrated and with and without CO₂ sequestration with varying Φ with experimental FFC parameters ($\eta_{fu} = 0.7$ and $\eta_{fc} = 0.5$).

The electrical efficiency of the FFCTH with and without sequestration changes at different Φ . At lower Φ , the electrical efficiency with and without CO₂ sequestration approach a similar value. This is primarily due to the higher fuel requirement at low Φ (Figure 7) and the power required for CO₂ sequestration in the CO₂ sequestration case compared to no CO₂ sequestration case, as Figure 9 shows. Due to this, the rate of increase of electrical efficiency is much faster for no sequestration case compared to the sequestration case. This shows that the amount of CO₂ generated affects the electrical efficiency reduction in the CO₂ sequestration case, which is in line with logic.

The maximum absolute efficiency penalty is 0.68% at $\Phi = 2.8$. This is a very small efficiency penalty compared to previous literature [36,37,48]. The electrical efficiency of the FFCTH without sequestration is 6.85% higher than the standard sCO₂ turbine setup without sequestration. The standard sCO₂ turbine setup pays a penalty of 1.44% for incorporating CO₂ sequestration.

Table 7 provides a comparison of previous attempts at integrating carbon sequestration with gas turbines. As shown from previous studies, conventional gas turbines typically have a 4–10% decrease in electrical efficiency when integrating post exhaust carbon capture and sequestration. Note that different systems use a variety of CO₂ sequestration methods, which leads to inconsistent efficiency penalties. The standard sCO₂ turbine suffers a smaller penalty in electrical efficiency based on the assumptions in this study, which include the exhaust heated air separation. As the waste heat rejection from the sCO₂ cycle is able to meet the air separation requirements in most cases, the efficiency penalty is small compared to previous work. Along with the fact that FFCTH system pays a much smaller penalty in efficiency; this system also provides an advantage over previous systems due to the high overall efficiency while being sequestration-ready.

Table 7. Comparison of electrical efficiency changes due to addition of carbon sequestration into the system in previous cases and current case.

Type of Power Generation Technique	Base Case Electrical Efficiency	Electrical Efficiency with CO ₂ Sequestration	Reference
Gas turbine	53.67	46.75	[36]
Gas turbine	43.88	35.26	[37]
Gas turbine +SOFC	Maximum of 69.5	Maximum of 65.7	[48]
sCO ₂ turbine	53.14	51.7	This work
sCO ₂ turbine + FFC	Maximum of 60	Maximum of 59.3	This work

We assumed earlier that the heat rejected by the system from the pre-cooler can provide heat for air separation. It is thus important to consider the P/H of the system to evaluate its ability to efficiently convert the incoming fuel energy to electricity compared to heat and make the system sequestration-ready. Since the parameters of the sCO₂ cycle are constant, the heat rejected from the pre-cooler is also constant at 4.81 MW.

Figure 11 shows the P/H of the proposed system with oxygen and with air and a comparison to a standard sCO₂ turbine system. The P/H of the FFCTH is greater than the standard sCO₂ turbine system at all Φ due to larger power generation. The P/H of the FFCTH with oxygen (sequestration-ready) is much higher than with air (not sequestration-ready) at all Φ . The highest P/H for sequestration-ready is 116 times that without at $\Phi = 2.8$. This is primarily because the oxygen separation uses most of the rejected heat from the sCO₂ cycle. Thus, minimum heat remains.

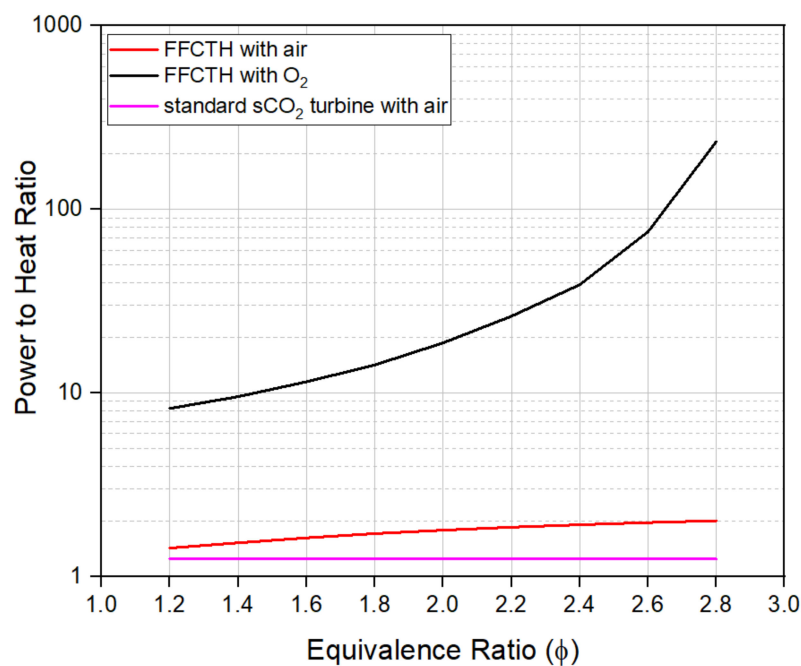


Figure 11. P/H ratios of the system with and without the FFC integrated with and without being CO₂ sequestration-ready at various Φ .

5. Conclusions and Future Work

In this paper, we provided a comprehensive analysis of a novel FFCTH. The system is novel in terms of its attractive efficiency without but also with sequestration-ready CO₂ emissions. The FFC provides heat for the sCO₂ cycle as opposed to a combustor in the standard sCO₂ cycle. Experimental characterization of the FFC assessed power density and efficiency. It also provided FFC parameters,

such as fuel utilization efficiency and fuel cell conversion efficiency, for a scaled up model and theoretical analysis.

The electrical efficiency of the FFCTH increases with increasing Φ with and without being CO₂ sequestration-ready. The electrical efficiency comparison of the FFCTH between sequestration-ready and not is only 0.68% lower at the Φ of 2.8. Surprisingly, this electrical efficiency is almost similar with and without CO₂ sequestration readiness at the Φ of 1.2 (0.03% lower with CO₂ sequestration ready case). The close match between the two cases occurs because waste heat can be utilized from the sCO₂ cycle. The electrical efficiency of the FFCTH reaches a maximum electrical efficiency of 60% at a Φ of 2.8. Although a penalty of lower electrical efficiency occurs with CO₂ sequestration, the proposed concept shows a lower reduction in electrical efficiency for carbon sequestration-ready power generation compared to previous literature due to the exhaust heat driven air separation. The proposed system suffers only a 0.68% penalty due to CO₂ sequestration. The results show that the syngas present in the fuel-rich combustion exhaust and the amount of CO₂ present in the exhaust are important factors in describing the results obtained.

The P/H ratio increases with increasing Φ . Furthermore, both with and without being sequestration-ready have greater P/Hs than the standard sCO₂ cycle. The P/H ratio of the FFCTH is 5.7 times higher at the Φ of 1.2 and 116 times higher at the Φ of 2.8 with CO₂ sequestration than without sequestration. The FFCTH minimizes unutilized heat from the system by using the rejected heat from sCO₂ turbine cycle. This shows a wide range of P/H ratios can be achieved by tuning system variables.

Several future studies can build upon this work. As examples, pressure loss, oxygen adsorption/desorption system size and issues with scaling up the experimental results can be addressed. Although the effect of pressure drop is not expected to significantly affect the conclusions of this study, it should be included in future analysis as it will reduce the performance slightly. The experimental results demonstrate the performance of a single fuel cell, but interconnect and other system losses can be considered with a scaled up experiment. In this study the use of waste heat was not considered except for the thermally-driven adsorption/desorption cycle. Other applications include integration with a steam/organic Rankine cycle, or for process heat, both of which can be investigated further.

Author Contributions: Conceptualization, E.B.S., I.E. and R.J.M.; Data curation, R.G.; Formal analysis, R.J.M.; Funding acquisition, E.B.S. and I.E.; Methodology, R.G., E.B.S. and R.J.M.; Project administration, R.J.M.; Supervision, R.J.M.; Writing—original draft, R.G.; Writing—review and editing, R.G., E.B.S., I.E. and R.J.M. All authors have read and agreed to the published version of the manuscript.

Funding: This research was funded by the USA Department of Energy's Office of Energy Efficiency and Renewable Energy (EERE) under the Solar Energy Technologies Office grant number DE-EE0008991.

Acknowledgments: This material is based upon work supported by the USA Department of Energy's Office of Energy Efficiency and Renewable Energy (EERE) under the Solar Energy Technologies Office Award Number DE-EE0008991. The views expressed herein do not necessarily represent the views of the USA Department of Energy or the USA Government.

Conflicts of Interest: The authors declare the following financial interests/personal relationships which may be considered as potential competing interests: A related invention disclosure was submitted.

References

1. U.S. Energy Information Administration. *Monthly Energy Review—January 2020*; 2020; Volume 35. Available online: <https://www.eia.gov/totalenergy/data/monthly/pdf/mer.pdf> (accessed on 23 September 2020).
2. Lueken, R.; Klima, K.; Griffin, W.M.; Apt, J. The climate and health effects of a USA switch from coal to gas electricity generation. *Energy* **2016**, *109*, 1160–1166. [[CrossRef](#)]
3. Bao, C.; Wang, Y.; Feng, D.; Jiang, Z.; Zhang, X. Macroscopic modeling of solid oxide fuel cell (SOFC) and model-based control of SOFC and gas turbine hybrid system. *Prog. Energy Combust. Sci.* **2018**, *66*, 83–140. [[CrossRef](#)]
4. Levi, M. Climate consequences of natural gas as a bridge fuel. *Clim. Chang.* **2013**, *118*, 609–623. [[CrossRef](#)]

5. De Gouw, J.A.; Parrish, D.D.; Frost, G.J.; Trainer, M. Reduced emissions of CO₂, NO_x, and SO₂ from U.S. power plants owing to switch from coal to natural gas with combined cycle technology. *Earth's Future* **2014**, *2*, 75–82. [[CrossRef](#)]
6. Hayhoe, K.; Kheshgi, H.S.; Jain, A.K.; Wuebbles, D.J. Substitution of natural gas for coal: Climatic effects of utility sector emissions. *Clim. Chang.* **2002**, *54*, 107–139. [[CrossRef](#)]
7. Venkatesh, A.; Jaramillo, P.; Griffin, W.M.; Matthews, H.S. Implications of changing natural gas prices in the United States electricity sector for SO₂, NO_x and life cycle GHG emissions. *Environ. Res. Lett.* **2012**, *7*, 034018. [[CrossRef](#)]
8. Bell, M.L.; Dominici, F. Effect modification by community characteristics on the short-term effects of ozone exposure and mortality in 98 US communities. *Am. J. Epidemiol.* **2008**, *167*, 986–997. [[CrossRef](#)]
9. Bell, M.L.; Ebisu, K.; Peng, R.D.; Walker, J.; Samet, J.M.; Zeger, S.L.; Dominici, F. Seasonal and Regional Short-term Effects of Fine Particles on Hospital Admissions in 202 US Counties, 1999–2005. *Am. J. Epidemiol.* **2008**, *168*, 1301–1310. [[CrossRef](#)]
10. Laden, F.; Schwartz, J.; Speizer, F.E.; Dockery, D.W. Reduction in fine particulate air pollution and mortality: Extended follow-up of the Harvard Six Cities Study. *Am. J. Respir. Crit. Care Med.* **2006**, *173*, 667–672. [[CrossRef](#)]
11. Pope, C.A.; Ezzati, M.; Dockery, D.W. Fine-particulate air pollution and life expectancy in the United States. *N. Engl. J. Med.* **2009**, *360*, 376–386. [[CrossRef](#)]
12. U.S. Environmental Protection Agency Office of Air and Radiation. *Regulatory Impact Analysis for the Final Clean Air Interstate Rule*; 2005. Available online: https://www.epa.gov/sites/production/files/2020-07/documents/transport_ria_final-clean-air-interstate-rule_2005-03.pdf (accessed on 23 September 2020).
13. Interconnection P. Coal Capacity at Risk for Retirement in PJM: Potential Impacts of the Finalized EPA Cross State Air Pollution Rule and Proposed National Emissions Standards for Hazardous Air Pollutants. 2011. Available online: <http://www.psc.ky.gov/PSCSCF/2011%20cases/2011-00401/Kentucky%20Power%20Responses%20to%20042312%20Order/AG/012712/AG%201-14%20Attachments/AG%201-14%20Attachment%207.pdf> (accessed on 23 September 2020).
14. Gaudernack, B.; Lynam, S. Natural gas utilisation without CO₂ emissions. *Energy Convers. Manag.* **1997**, *38*, S165–S172. [[CrossRef](#)]
15. O'Hayre, R.; Cha, S.-W.; Colella, W.; Prinz, F.B. *Fuel Cell Fundamentals*; Intergovernmental Panel on Climate Change, Ed.; John Wiley & Sons, Inc.: Hoboken, NJ, USA, 2016; ISBN 9781119191766.
16. Milcarek, R.J.; Garrett, M.J.; Welles, T.S.; Ahn, J. Performance investigation of a micro-tubular flame-assisted fuel cell stack with 3,000 rapid thermal cycles. *J. Power Sources* **2018**, *394*, 86–93. [[CrossRef](#)]
17. Du, Y.; Finnerty, C.; Jiang, J. Thermal Stability of Portable Microtubular SOFCs and Stacks. *J. Electrochem. Soc.* **2008**, *155*, B972. [[CrossRef](#)]
18. Wang, Y.; Zeng, H.; Cao, T.; Shi, Y.; Cai, N.; Ye, X.; Wang, S. Start-up and operation characteristics of a flame fuel cell unit. *Appl. Energy* **2016**, *178*, 415–421. [[CrossRef](#)]
19. Wang, Y.; Shi, Y.; Ni, M.; Cai, N. A micro tri-generation system based on direct flame fuel cells for residential applications. *Int. J. Hydrogen Energy* **2014**, *39*, 5996–6005. [[CrossRef](#)]
20. Kronmayer, H.; Barzan, D.; Horiuchi, M.; Sukanuma, S.; Tokutake, Y.; Schulz, C.; Bessler, W.G. A direct-flame solid oxide fuel cell (DFFC) operated on methane, propane, and butane. *J. Power Sources* **2007**, *166*, 120–126. [[CrossRef](#)]
21. Vogler, M.; Horiuchi, M.; Bessler, W.G. Modeling, simulation and optimization of a no-chamber solid oxide fuel cell operated with a flat-flame burner. *J. Power Sources* **2010**, *195*, 7067–7077. [[CrossRef](#)]
22. Horiuchi, M.; Sukanuma, S.; Watanabe, M. Electrochemical Power Generation Directly from Combustion Flame of Gases, Liquids, and Solids. *J. Electrochem. Soc.* **2004**, *151*, A1402. [[CrossRef](#)]
23. Wang, K.; Milcarek, R.J.; Zeng, P.; Ahn, J. Flame-assisted fuel cells running methane. *Int. J. Hydrogen Energy* **2015**, *40*, 4659–4665. [[CrossRef](#)]
24. Milcarek, R.J.; Garrett, M.J.; Wang, K.; Ahn, J. Micro-tubular flame-assisted fuel cells running methane. *Int. J. Hydrogen Energy* **2016**, *41*, 20670–20679. [[CrossRef](#)]
25. Milcarek, R.J.; Wang, K.; Falkenstein-Smith, R.L.; Ahn, J. Micro-tubular flame-assisted fuel cells for micro-combined heat and power systems. *J. Power Sources* **2016**, *306*, 148–151. [[CrossRef](#)]
26. Milcarek, R.J.; Ahn, J. Rich-burn, flame-assisted fuel cell, quick-mix, lean-burn (RFQL) combustor and power generation. *J. Power Sources* **2018**, *381*, 18–25. [[CrossRef](#)]

27. Milcarek, R.J.; Garrett, M.J.; Baskaran, A.; Ahn, J. Combustion Characterization and Model Fuel Development for Micro-tubular Flame-assisted Fuel Cells. *J. Vis. Exp.* **2016**, *116*, e54638. [[CrossRef](#)] [[PubMed](#)]
28. Milcarek, R.J.; Nakamura, H.; Tezuka, T.; Maruta, K.; Ahn, J. Microcombustion for micro-tubular flame-assisted fuel cell power and heat cogeneration. *J. Power Sources* **2019**, *413*, 191–197. [[CrossRef](#)]
29. Ghotkar, R.; Milcarek, R.J. POWER2019-1852 Integration of Flame-assisted Fuel Cells with a Gas Turbine running Jet-A as fuel. In Proceedings of the ASME 2019 Power Conference collocated the ASME 2019 Nuclear Forum (POWER2019), Salt Lake City, UT, USA, 15–18 July 2019; pp. 1–9.
30. Milcarek, R.J.; Ahn, J. Micro-tubular flame-assisted fuel cells running methane, propane and butane: On soot, efficiency and power density. *Energy* **2019**, *169*, 776–782. [[CrossRef](#)]
31. Milcarek, R.J.; DeBiase, V.P.; Ahn, J. Investigation of startup, performance and cycling of a residential furnace integrated with micro-tubular flame-assisted fuel cells for micro-combined heat and power. *Energy* **2020**, *196*, 117148. [[CrossRef](#)]
32. Ghotkar, R.; Milcarek, R.J. Investigation of flame-assisted fuel cells integrated with an auxiliary power unit gas turbine. *Energy* **2020**, *204*, 117979. [[CrossRef](#)]
33. Olajire, A.A. A review of mineral carbonation technology in sequestration of CO₂. *J. Pet. Sci. Eng.* **2013**, *109*, 364–392. [[CrossRef](#)]
34. Gunning, P.J.; Hills, C.D.; Carey, P.J. Accelerated carbonation treatment of industrial wastes. *Waste Manag.* **2010**, *30*, 1081–1090. [[CrossRef](#)]
35. Eloneva, S.; Teir, S.; Salminen, J.; Fogelholm, C.J.; Zevenhoven, R. Fixation of CO₂ by carbonating calcium derived from blast furnace slag. *Energy* **2008**, *33*, 1461–1467. [[CrossRef](#)]
36. Cormos, C.C. Integrated assessment of IGCC power generation technology with carbon capture and storage (CCS). *Energy* **2012**, *42*, 434–445. [[CrossRef](#)]
37. Tola, V.; Pettinau, A. Power generation plants with carbon capture and storage: A techno-economic comparison between coal combustion and gasification technologies. *Appl. Energy* **2014**, *113*, 1461–1474. [[CrossRef](#)]
38. Ermanoski, I.; Stechel, E.B. Thermally-driven adsorption/desorption cycle for oxygen pumping in thermochemical fuel production. *Sol. Energy* **2020**, *198*, 578–585. [[CrossRef](#)]
39. Bray, J.M.; Schneider, W.F. Potential energy surfaces for oxygen adsorption, dissociation, and diffusion at the Pt(321) surface. *Langmuir* **2011**, *27*, 8177–8186. [[CrossRef](#)]
40. Rochau, G.E.; Pasch, J.J.; Cannon, G.; Carlson, M.; Fleming, D.; Kruizenga, A.; Sharpe, R.; Wilson, M. Supercritical CO₂ Brayton Cycles. 2014. Available online: <https://www.osti.gov/servlets/purl/1221819> (accessed on 23 September 2020).
41. Seo, Y.; Huh, C.; Lee, S.; Chang, D. Comparison of CO₂ liquefaction pressures for ship-based carbon capture and storage (CCS) chain. *Int. J. Greenh. Gas Control* **2016**, *52*, 1–12. [[CrossRef](#)]
42. Milcarek, R.J.; Garrett, M.J.; Ahn, J. Micro-tubular flame-assisted fuel cells. *J. Fluid Sci. Technol.* **2017**, *12*, JFST0021. [[CrossRef](#)]
43. McBride, B.J.; Gordon, S.; McBride, B.J. Computer Program for Calculation of Complex Chemical Equilibrium Compositions and Applications. *NASA Ref. Publ.* **1994**, *1311*, 184. Available online: https://web.stanford.edu/~cantwell/AA284A_Course_Material/AA284A_Resources/NASA_Glenn_Reports/McBride%20and%20Gordon,%20Computer%20Program%20for%20Calculation%20of%20Complex%20Chemical%20Equilibrium%20NASA%20RP%201311%201996%20Part%20II.pdf (accessed on 23 September 2020).
44. Speight, J.G. *Natural Gas*; Elsevier: Amsterdam, The Netherlands, 2007; ISBN 9781933762142.
45. Milcarek, R.J.; Wang, K.; Garrett, M.J.; Ahn, J. Performance Investigation of Dual Layer Yttria-Stabilized Zirconia–Samaria-Doped Ceria Electrolyte for Intermediate Temperature Solid Oxide Fuel Cells. *J. Electrochem. Energy Convers. Storage* **2016**, *13*, 011002. [[CrossRef](#)]
46. Zeng, H.; Gong, S.; Shi, Y.; Wang, Y.; Cai, N. Micro-tubular solid oxide fuel cell stack operated with catalytically enhanced porous media fuel-rich combustor. *Energy* **2019**, *179*, 154–162. [[CrossRef](#)]

47. Lemmon, E.W.; Bell, I.H.; Huber, M.L.; McLinden, M.O. *NIST Standard Reference Database 23: Reference Fluid Thermodynamic and Transport Properties-REFPROP*; Version 9.1; National Institute of Standards and Technology: Gaithersburg, MD, USA, 2013; Volume 135.
48. Park, S.K.; Kim, T.S.; Sohn, J.L.; Lee, Y.D. An integrated power generation system combining solid oxide fuel cell and oxy-fuel combustion for high performance and CO₂ capture. *Appl. Energy* **2011**, *88*, 1187–1196. [[CrossRef](#)]



© 2020 by the authors. Licensee MDPI, Basel, Switzerland. This article is an open access article distributed under the terms and conditions of the Creative Commons Attribution (CC BY) license (<http://creativecommons.org/licenses/by/4.0/>).